



https://doi.org/10.30678/fjt.126885

© 2023 The Authors

Open access (CC BY 4.0)

Influence of the Bowtie Shaped Dimples on the Performance of Sliding Surfaces under Hydrodynamic Lubrication

Hardik Gangadia¹, Saurin Sheth²

¹Gujarat Technological University, Ahmedabad, India

²G. H. Patel College of Engineering & Technology – V. V. Nagar, Gujarat, India

Corresponding author: Hardik Gangadia (hgangadia@gmail.com)

ABSTRACT

It covers the tribological behaviour of sliding surfaces, one of which has bowtie-shaped micro-dimples. Against the other fixed, textured wall, one wall is smooth and moving at a constant speed. For the formation of hydrodynamic pressure and tribological behaviour, the effects of bowtie-shaped dimples and orientated bowtie-shaped dimples have been compared with circular-shaped dimples. Additionally, the impact of sliding speed, dimple area density, and dimple depth on tribological behaviour was examined. The findings show that compared to a circular-shaped dimple, an atypical bowtie-shaped and orientated bowtie-shaped dimple generates a higher net hydrodynamic pressure in the fluid domain and offers improved stability between the sliding surfaces. It has been demonstrated that geometrical factors like dimple depth and area density as well as operational factors like sliding speed have a substantial impact on the hydrodynamic average pressure and tribological behaviour of sliding surfaces. The experimental results support the conclusions from the analysis and CFD.

Keywords: Surface Texturing, Tribological Behaviour, Hydrodynamic Lubrication, Sliding Surfaces, CFD

1. Introduction:

To improve the tribological behaviour of sliding surfaces, hydrodynamic lubrication between sliding surfaces is crucial in components like journal bearings and mechanical seals. Numerous studies have been conducted to increase the hydrostatic and hydrodynamic load capacities of sliding surfaces. The impacts of coning, misalignment, waviness, and hydropads have been

discovered to generate positive pressure and increase the load capacity of sliding surfaces [1-6].

Laser texturing has been a dependable method for mechanical components over the past 20 years. An increase in hydrodynamic pressure and load carrying capacity as well as a decrease in generated friction and wear are shown when one of the sliding surfaces is given surface texturing. Numerous applications of surface texturing are now being

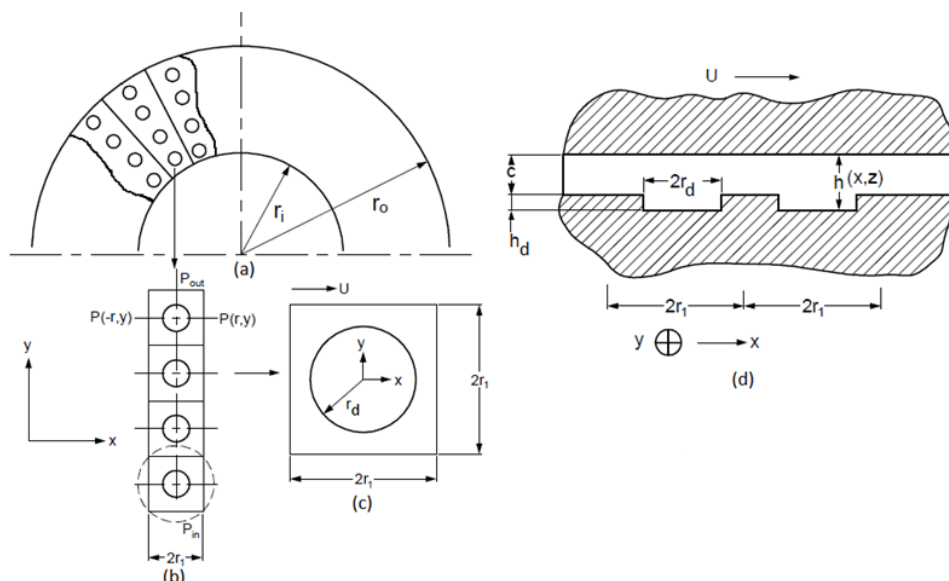


Figure 1: Geometric model of laser textured mechanical seal

employed to assist tribology. Shot blasting [7], laser texturing [8–9], reactive ion etching [10], and micro-electrolytic etching [11] are only a few of the surface texturing methods that are currently accessible. Compared to other methods, laser texturing provides unparalleled control over the surface microstructure and minimal environmental impact.

The fluid is propelled forward when the upper surface slides as a result of the relative motion between sliding surfaces. Diverging action causes the pressure to decrease as the fluid goes into the dimple while converging action causes the pressure to rise as the fluid leaves the dimple. The load-bearing capacity between the sliding surfaces is increased by the difference between pressure drop and rise, which generates a net positive pressure.

A mechanical seal model with a hemispherical regular micro-surface on one of the mating seal faces was presented by Etsion & Burstein [12], improving seal performance through lower friction. According to Etsion et al. [13–14], the fluid film stiffness is maximized in laser-textured surfaces with optimal pore depth over pore diameter. Circular micro dimples [12–16] have been the main focus of analysis to date since they are simple to produce. Few researches [18–19] discovered that an elliptical dimple positioned perpendicular to the direction of sliding gave the highest result of load carrying capacity whereas some researchers [17–20] concentrated on conventionally shaped micro dimples such as square, triangle, and ellipse. For the case of a gas-lubricated parallel sliding bearing, Qui et al. [21] optimized the texture geometry and density of six different dimple shapes for maximum load carrying capacity. They came to the conclusion that the ellipsoidal dimple shape results in the highest load carrying capacity and that the optimal geometry and density are almost independent of the operating conditions. Then Qui et al. [22] adjusted the texture geometry and density of six distinct dimple forms in order to achieve the lowest friction coefficient and best bearing stiffness, and they reported that the ellipsoidal shape produced the lowest friction coefficient and highest bearing stiffness. Dimple area density has been identified by Yan et al. [11] and Raeymaekers et al. [23] as another important factor influencing the tribological behaviour of sliding surfaces.

The pressure and velocity distribution features of the lubricant flow between textured sliding surfaces are currently being calculated by many studies [24–27] using commercial CFD Programmes like FLUENT. Liu et al. [26] recently used numerical modelling to examine the effects of spherical micro-dimples' geometric and operational characteristics on the tribological performance of textured surfaces and suggested utilizing a dimple area density of 25–35% in practical applications. A numerical analysis was conducted by Wei et al. [27] to determine the impact of geometric features for various dimple shapes on pressure build-up. Additionally, a new parameter known as dimple surface angle was added in this article, and it was discovered that changes are most noticeable when the

dimple surface angle is less than 30°. The load carrying capability of a single typical dimple shape (e.g., circular, square, triangle, spherical, etc.) has received a lot of attention up to this point, but the tribological effects of texturing with unconventional shapes have not received as much attention. However, unconventional dimple forms cannot be disregarded because they offer superior tribological benefits than traditional dimple shapes and offer more convergence opportunities.

An analytical model is offered to forecast the hydrodynamic pressure production for the application of a laser-textured mechanical seal followed by CFD analysis in this work to examine the impact of straight and orientated bowtie-shaped dimples over circular shaped dimples. The experimental results and those from the analytical approach and CFD were in good agreement. Measurements of coefficient of friction was made for the parametric analysis in order to examine the effects of various geometrical factors, including dimple depth and area density, as well as operational factors, such sliding speed, on hydrodynamic pressure.

2. Analytical Model:

Figure 1 shows the geometrical model of a mechanical seal with laser texturing. The seal ring's inner and outer radii are designated as r_i and r_o , respectively, and the corresponding values have been taken as 0.0181 m and 0.0235 m. The parameters of each dimple are depth h_d and radius r_d . On one of the seal's faces, there are a uniform distribution of laser-textured dimples. As shown in Figure 1(c), each dimple is modelled at the center of an imaginary square cell with a length of $2r_1$. Length of the imaginary square cell with relation to circular dimple area density S_p ,

$$2r_1 = \sqrt{\frac{\pi}{S_d}} \times r_d \quad (1)$$

The bowtie-section of the textured seal is depicted in Figure 1(d). The seal has two sides, one of which has a micro-texture and the other of which is flat. The relative velocity of a flat surface to a textured surface is U . According to the diagram, $h(x,z)$ represents the local distance and c represents the minimum distance between the bearing surfaces, where x and z are Cartesian coordinates. It is assumed that an incompressible viscous fluid separates the seal faces.

For a mechanical seal, the generalized Reynolds' equation is expressed as,

$$\frac{\partial}{\partial x} \left(h^3 \frac{\partial p}{\partial x} \right) + \frac{\partial}{\partial z} \left(h^3 \frac{\partial p}{\partial z} \right) = 6\mu U \frac{\partial h}{\partial x} \quad (2)$$

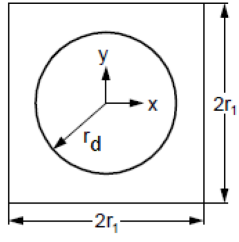
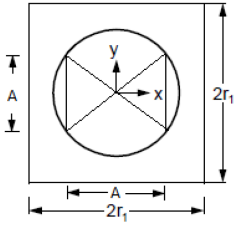
Modified Reynold's equation in order to deal with cavitation is,

$$\frac{\partial}{\partial x} \left(K\beta h^3 \frac{\partial \xi}{\partial x} \right) + \frac{\partial}{\partial z} \left(K\beta h^3 \frac{\partial \xi}{\partial z} \right) = 6\mu U \frac{\partial(\xi h)}{\partial x} \quad (3)$$

Dimensionless Reynold's equation is,

$$\frac{\partial}{\partial X} \left(KH^3 \frac{\partial \xi}{\partial X} \right) + \frac{\partial}{\partial Z} \left(KH^3 \frac{\partial \xi}{\partial Z} \right) = \Lambda \frac{\partial \xi H}{\partial X} \quad (4)$$

Table 1: Details of all dimple shaped geometries

Shape	Equivalent Dimensions	Cell Size	Conditions for film thickness H(X,Y)
 <p>Circular</p>	$r_d = \sqrt{\frac{A_{circle}}{S_d}}$	$2r_1 = \sqrt{\frac{\pi}{S_d}} \times r_d$	$\begin{cases} 1 + \frac{\epsilon}{\delta} & \text{if } X^2 + Y^2 \leq 1 \\ 1 & \text{if } X^2 + Y^2 > 1 \end{cases}$
 <p>Bowtie</p>	$A = \sqrt{2\pi} \times r_p$	$2r_1 = \sqrt{\frac{A^2}{2S_p}}$	$\begin{cases} 1 + \frac{\epsilon}{\delta} & \text{if } Y \leq X \leq \frac{1}{\sqrt{2}} \\ 1 & \text{else} \end{cases}$

Assuming that micro-dimples are uniformly distributed, only one radial column of dimples is taken into account. Figure 1(b) illustrates the boundary condition for one radial column.

$$\begin{aligned} p(x, z = r_i) &= p_{in} \\ p(x, z = r_o) &= p_{out} \end{aligned} \tag{5}$$

In this approach, the pressure distribution is presumptively periodic in the circumferential direction with a period equal to the square cell's hypothetical length. As a result, the pressure is exerted on a periodic basis in the direction of the circumference.

$$p(x = -r_1, z) = p(x = r_1, z) \tag{6}$$

Boundary conditions in dimensionless form are given as follows,

$$\begin{aligned} P\left(X, Z = \frac{r_i}{r_d}\right) &= \frac{p_{in}}{p_a} \\ P\left(X, Z = \frac{r_o}{r_d}\right) &= \frac{p_{out}}{p_a} \\ P\left(X = -\frac{r_1}{r_d}, Y\right) &= P\left(X = \frac{r_1}{r_d}, Y\right) \end{aligned} \tag{7}$$

This work considers the fabrication of LST-based circular, bowtie, and orientated bowtie-shaped dimples. All dimples are symmetric to the XZ plane, have flat bottoms, and flat boundary walls. In Table 1, the bowtie-shaped dimple's shape geometry, equivalent dimple dimension in relation to area of circular dimple, cell size, and dimensionless local separation H(X,Y) between textured and flat surfaces within one unit cell are all described.

A finite difference approach with an over relaxation factor of 1.4 can be used to solve Equation 3 for the

pressure distribution in the seal clearance. Based on convergence and precision, a uniform 100 x 100 node Cartesian grid is chosen. By integrating the pressure over the seal region, one can obtain the opening force necessary to prevent contact between the seal faces. In analysis and experimental work, SAE 30 oil, which has a dynamic viscosity of 0.29 kg/m.s at 20 °C and a density of 875 kg/m³, was used.

3. CFD Model:

Prior to the experimental work, CFD analysis was conducted to confirm the conclusions drawn from the analytical model. Reconstructed Figure 1(d) is displayed as Figure 2, which depicts the geometric parameters of the CFD model. 2r₁ stands for the domain length, which will be constant throughout all analyses. Quantity h_d is the depth of the dimple, and quantity c is the fluid film thickness, which is predetermined.

The same graphic also depicts the fluid domain's boundary conditions. Both the upper and bottom walls of the fluid experience no slip condition. A periodic boundary condition confines edges in the x-direction. The top wall, which has an untextured surface, is sliding with constant velocity U in the x-direction while the bottom wall is motionless. According to Figure 3, circular, bowtie, and orientated bowtie dimple shapes are created and modelled for the hydrodynamic study.

Between sliding pairs, lubricant is supplied and treated as an incompressible Newtonian fluid with constant viscosity, density, and body force. It is believed that flow is laminar and isothermal. Additionally, it is believed that the impact of a solid structure developing as a result of fluid pressure is minimal. The lubricant flow is governed by Navier-Stokes (momentum) equations and continuity equation, which can be written respectively,

$$\rho(\mathbf{v} \cdot \nabla)\mathbf{v} = -\nabla p + \nabla \cdot (\mu \nabla \mathbf{v}) \tag{8}$$

$$\nabla \cdot \mathbf{v} = 0 \tag{9}$$

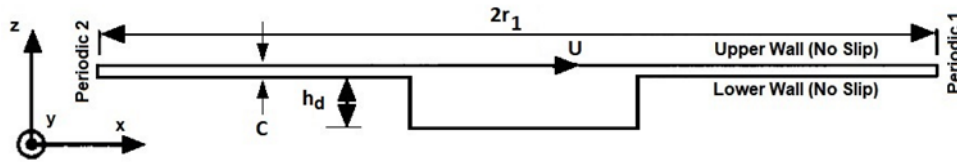


Figure 2: Geometric parameters and boundary conditions of model

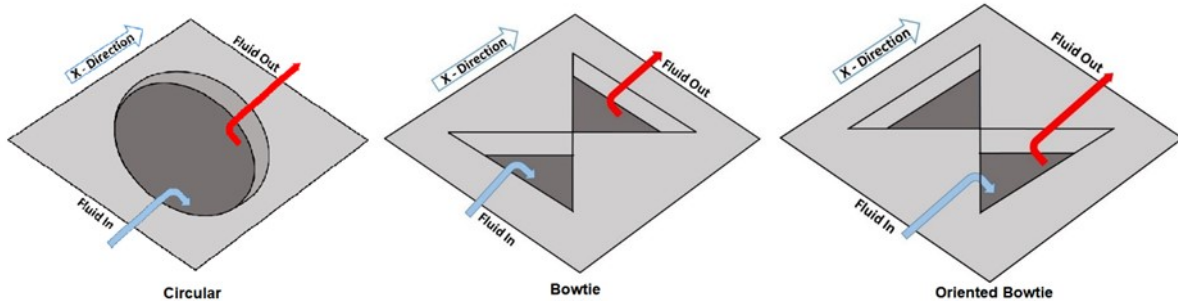


Figure 3: Designs of dimple shapes

The pressure distribution of lubricant between sliding pairs was calculated using the commercial CFD tool FLUENT. The development of cavitation produced inside the dimples is believed to be connected to the process for improved performance in developing the hydrodynamic pressure in textured sliding surfaces. In this case, the pressure in the lubricant may drop below the gas saturation pressure at the diverging zone, causing cavitation to occur. The Rayleigh-Plesset multi-phase cavitation model [28], which has been successfully tested in references [29–30], is employed. When pressure drops below the saturation pressure in this multi-phase model, lubricant vapour is created. In order to make it simple to compare various outcomes, results are obtained in dimensional form but are presented in nondimensional form.

4. Experimental Setup:

The pin-on-disc wear testing apparatus, which is schematically depicted in Figure 4, was used for all of the studies. With the aid of a motor, the lower disc can be rotated at any speed between 100 and 2000 revolutions per minute. The EN31 disc has a diameter of 165 mm and a thickness of 8 mm. A metallic holder that provides self-alignment and vertical loading is fixed to a textured pin. A

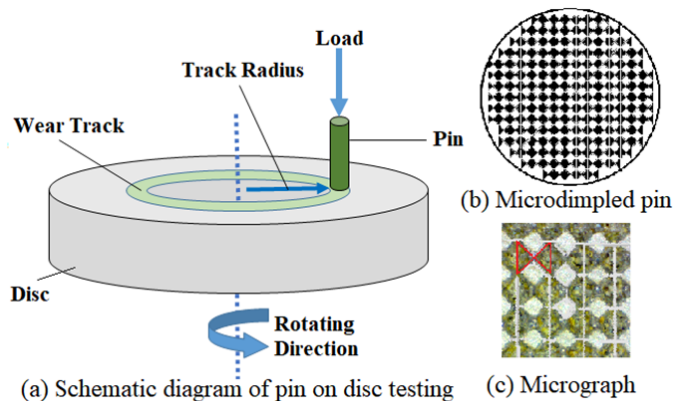


Figure 4: Experimental Setup & Specimen Preparation

sensor that measures the coefficient of friction is fastened to the textured pin. Every piece of data that comes in from sensors is collected on a computer by an acquisition system.

4.1 Specimen Preparation

The contact area between the pin and the disc is 78.5 mm², and the cylindrical textured pin is 10 mm x 30 mm in size. Using a laser marking device, pins are given texture. By adjusting the laser power and the number of laser passes, dimple depth can be regulated. Pins with a cylindrical texture are made of EN31 material and are texturized. Following polishing and optical flattening, the flatness of each pin was examined under a monochromatic check light. According to Figure 4(b), there are evenly spaced micro-dimples throughout the pin. The pins were cleaned with a cleaner before each trial, and the weight of each pin was determined using an electronic digital weighing machine.

4.2 Test Procedure

First, a metallic holder was used to place the textured pin for the test, and then the lubricant flow was initiated. Track radius is maintained at 40 mm. The motor is started once the lubrication level is reached. As a lubricant, SAE 30 oil is used. Then, under various loading situations and speeds, the values of coefficient of friction were recorded. The textured pin is changed out for the new one when the test is over.

5. Results and Discussion

The impact of dimple shape, geometrical parameters like dimple depth and area density, and operational parameters like sliding speed are all addressed here. Furthermore, the results of the experimental study are discussed in detail.

5.1 Effect of Dimple Shape

Figure 5 shows pressure distributions for circular

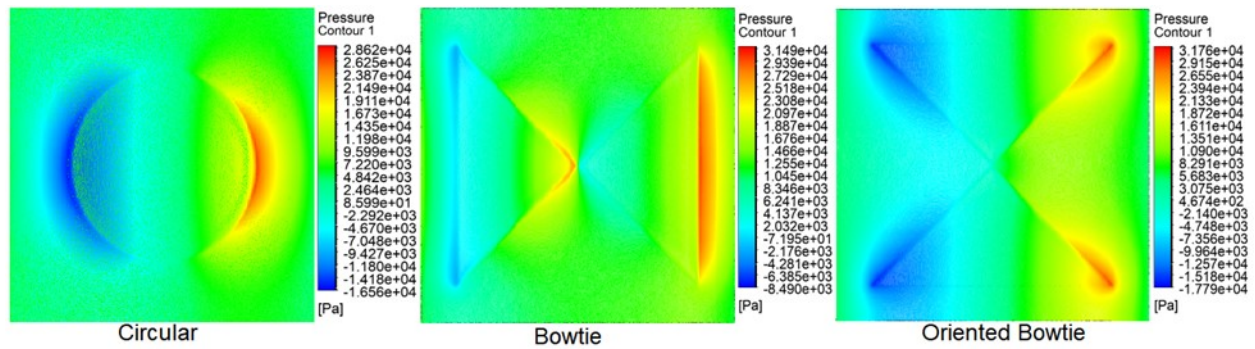


Figure 5: Pressure distribution in the fluid domain for different shapes

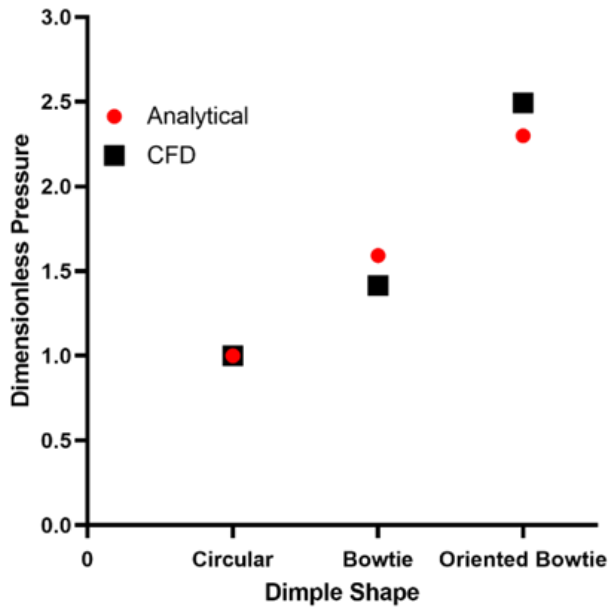


Figure 6: Comparison of dimensionless average pressure

dimple, bowtie dimple, and bowtie dimple positioned at a 90-degree angle. To make it simple to compare the findings, all variables are kept at the same value throughout the simulation for each shape, such as sliding speed (U) = 6 m/s, dimple depth (h_p) = 15 μm , dimple area density = 30%, and fluid film thickness (c) = 2 μm . Figure 5 clearly shows that the pressure decreases initially owing to divergence as the fluid flows along the x-direction and enters the dimple. The pressure then increases as the fluid advances due to the dimple's convergence, and because this generated pressure is greater than the pressure drop during divergence, a net positive pressure is ultimately produced. The change in this net pressure can only be attributed to the different geometric shapes of the dimple because all other geometric and operational parameters have been kept constant. However, in terms of generating hydrodynamic pressure, geometric characteristics like dimple depth and area density as well as operational parameters like sliding speed are also crucially important.

Figure 6 compares the dimensionless average pressure for the various dimple shapes taken into consideration in this paper. The graphic clearly shows that there is a significant correlation between the findings of the

analytical investigation and the CFD study. The bowtie-shaped dimple generates about 40% more hydrodynamic pressure and the orientated bowtie-shaped dimple generates about 150% more hydrodynamic pressure than the circular-shaped dimple for the values of the geometric and operating parameters mentioned above. This is certainly due to the strong convergence near the dimple's periphery.

5.2 Effect of Dimple Depth

Figure 7 displays the pressure distributions for a bowtie dimple and an orientated bowtie dimple at their minimum and maximum depths. To accurately reflect the hydrodynamic effect of depth for bowtie and orientated bowtie dimples, all other factors are kept constant. The graphic makes it evident that convergence happens in two stages in bowtie-shaped dimple and also in orientated bowtie-shaped dimple, convergence is more efficient than in the case of circular-shaped dimple, leading to higher hydrodynamic pressure generation.

Figure 8 presents the dimensionless pressure as a function of the depth of the dimples for 2 different loading conditions. In the case of circular dimples, it has been found that the dimensionless pressure rises as the depth of the dimple increases. While the highest pressure for bowtie dimples is reached at a depth of 10 μm , and pressure drops as depth increases. For orientated bowtie dimples, dimensionless pressure stays nearly constant for all dimple depths. It has been found that bowtie dimples generate the maximum pressure at a depth of 10 μm , whereas orientated bowtie-shaped dimples generate the highest pressure at all other depths. It is clear from this that dimple depth has a significant impact on the generation of hydrodynamic pressure.

To comprehend the implications of dimple depth on tribological performance, the pressure distribution of the lubricant is examined. Figures 9 to 11 show the pressure distribution of various dimple shapes along the x axis at various depths, while Figures 12 to 14 show the pressure distribution of various dimple shapes along the y axis at different depths. Pressure decreases as the liquid enters the dimple and then rises as it moves further in the x direction due to convergence.

It is evident that the maximum positive pressure is higher than the maximum negative pressure. As a result, the net pressure rises and friction coefficient decreases as a

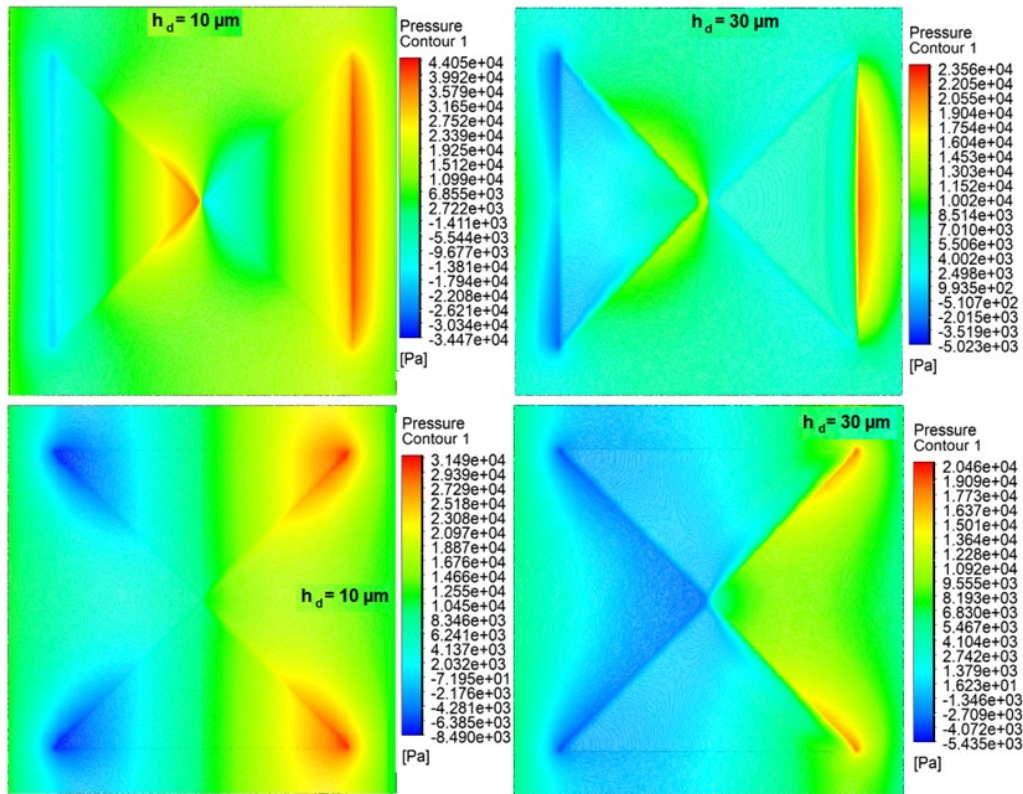


Figure 7: Pressure distribution in the fluid domain for different depths

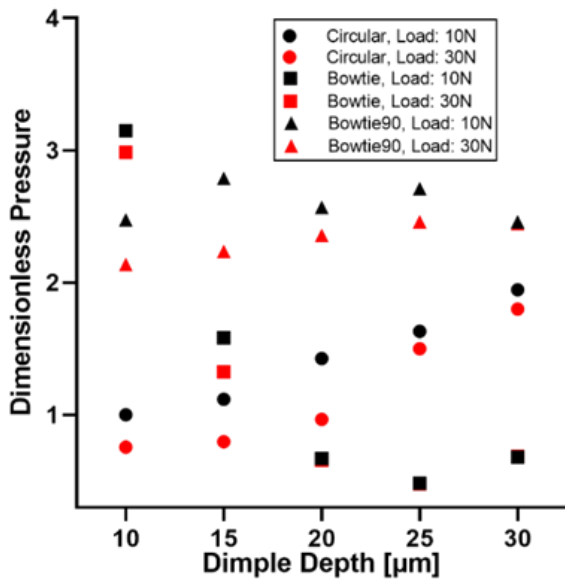


Figure 8: Dimensionless pressure as a function of dimple depth

result of an increase in load carrying capacity. Figures 9 to 11 show that stability between the sliding surfaces rises and the difference between negative and positive pressure in the x direction diminishes as the dimple depth increases. It is noticeable that a bowtie-shaped dimple with a 10μm dimple depth produces the maximum hydrodynamic pressure. Additionally, it is noted that for each dimple depth case, bowtie-shaped dimples exhibit two waves of pressure distribution in the same dimple length span,

improving the stability of the sliding surfaces. If we talk about the pressure distribution in the Y direction, Figures 12 to 14 show that for each dimple depth taken, bowtie-shaped dimples have a more uniform pressure distribution than circular-shaped dimples and oriented bowtie-shaped dimples, which provides more stability in the Y direction as well.

5.3 Effect of Dimple Area Density

Figure 15 displays the pressure distributions for the bowtie dimple and the oriented bowtie dimple's minimum and maximum dimple area density. To accurately represent the hydrodynamic effect of dimple area density for bowtie and orientated bowtie dimples, all other factors are kept constant. As discussed earlier, it is clear from this figure too that convergence happens in two stages in bowtie-shaped dimple. Convergence is also more significant in oriented bowtie-shaped dimple than in the case of circular-shaped dimple, leading to higher hydrodynamic pressure generation.

Figure 16 presents the dimensionless pressure as a function of the dimple area density of the dimples for 2 different loading conditions. In the case of circular dimples, it has been found that the dimensionless pressure drops as the dimple area density increases. The highest pressure for bowtie dimples is obtained when dimple area density is kept to 40%, and pressure drops as dimple area density decreases. For oriented bowtie dimples, dimensionless pressure stays nearly constant for all dimple area densities. It has been found that bowtie dimples generate the maximum pressure at an area density of 40%,

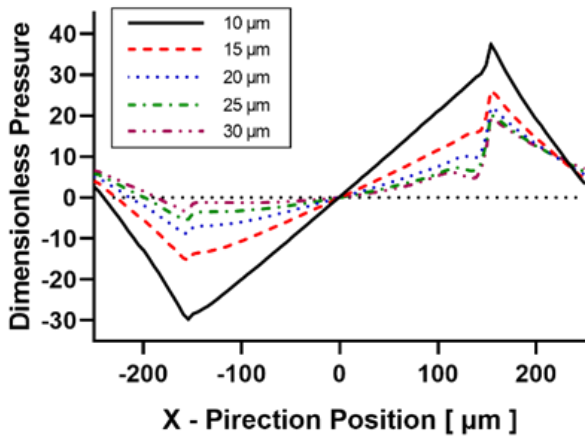


Figure 9: Effect of dimple depth on pressure distribution along x-direction (for circular dimple)

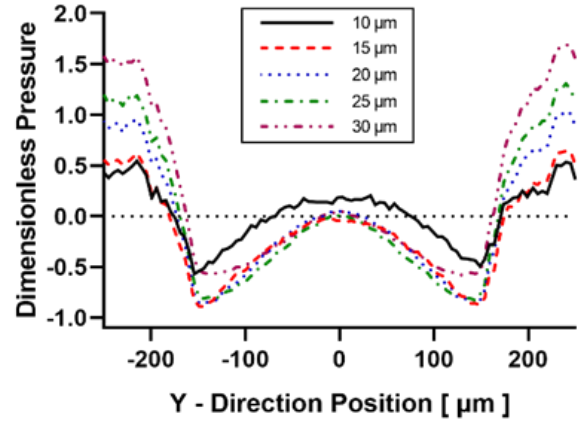


Figure 12: Effect of dimple depth on pressure distribution along y-direction (for circular dimple)

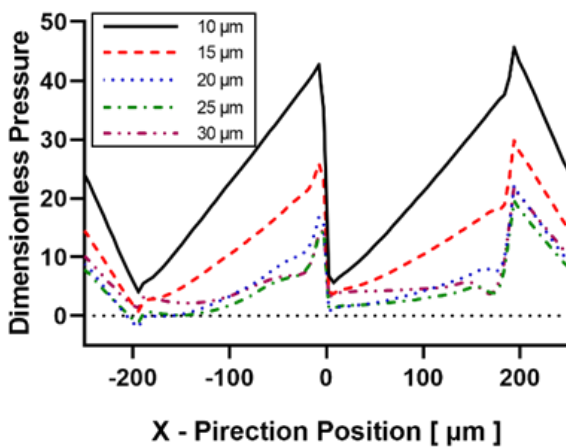


Figure 10: Effect of dimple depth on pressure distribution along x-direction (for bowtie dimple)

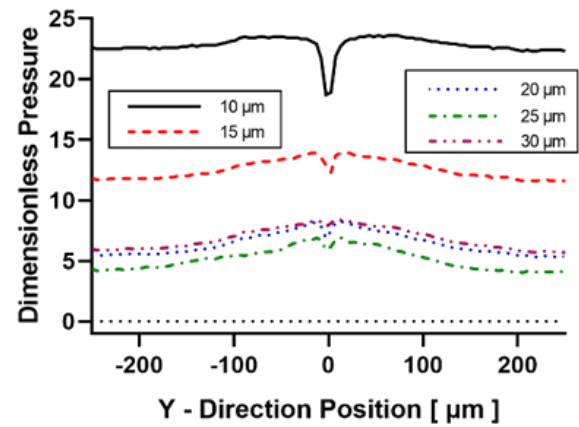


Figure 13: Effect of dimple depth on pressure distribution along y-direction (for bowtie dimple)

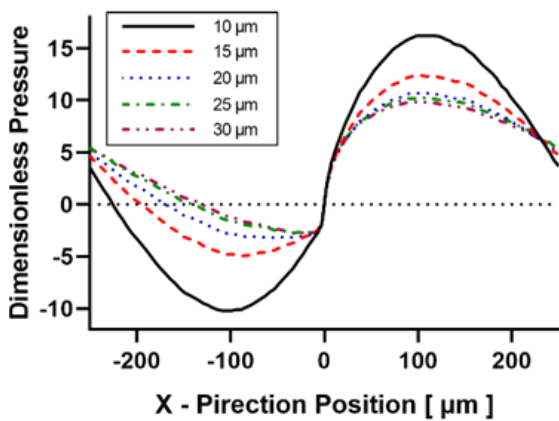


Figure 11: Effect of dimple depth on pressure distribution along x-direction (for oriented bowtie dimple)

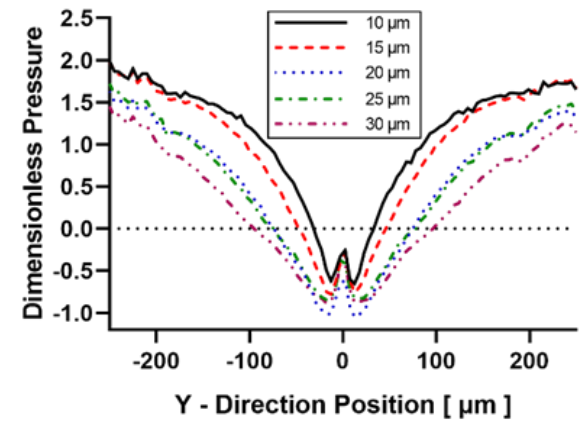


Figure 14: Effect of dimple depth on pressure distribution along y-direction (for oriented bowtie dimple)

whereas orientated bowtie-shaped dimples generate the highest pressure at all other area densities. It is clear from this that dimple density has a significant impact on the generation of hydrodynamic pressure.

The lubricant pressure distribution is used to investigate how the density of the dimples affects tribological performance. Figures 17 to 19 show the

pressure distribution of various dimple forms along the x axis at various densities of dimples, while Figures 20 to 22 show the pressure distribution of various dimple shapes along the y axis at various densities of dimples. As was already established, as the liquid enters the dimple, the pressure switches to a negative value and rises as a result of convergence as it moves further in the x direction.

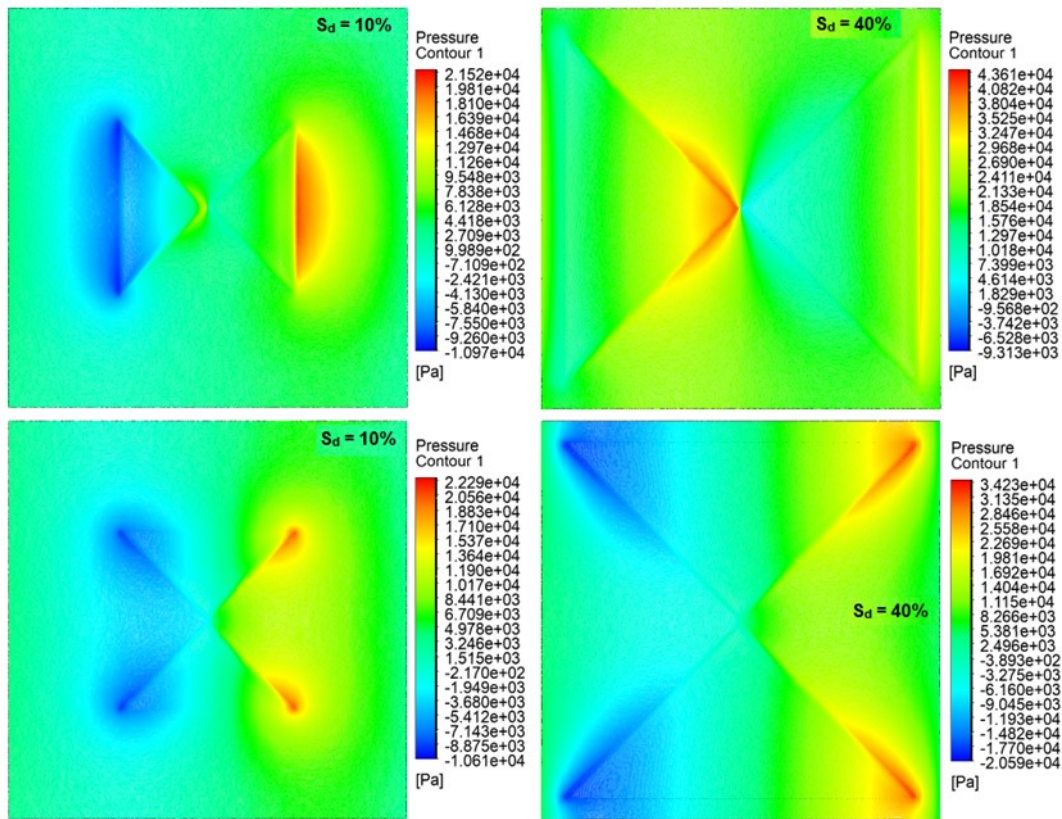


Figure 15: Pressure distribution in the fluid domain for different dimple area density

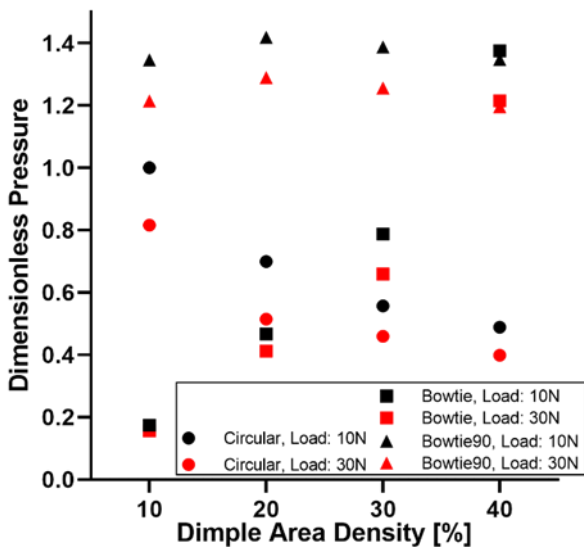


Figure 16: Dimensionless pressure as a function of dimple area density

As stated earlier the maximum positive pressure is higher than the maximum negative pressure. As a result, the net pressure rises and friction coefficient decreases as a result of an increase in load carrying capacity. Figures 17 to 19 show that stability between the sliding surfaces reduces and the difference between negative and positive pressure in the x direction increases as the dimple area density increases. It is noticeable that a bowtie-shaped dimple with

a 40% dimple area density produces the maximum hydrodynamic pressure. Here also it is noted that for each dimple area density case, bowtie-shaped dimples exhibit two waves of pressure distribution in the same dimple length span, improving the stability of the sliding surfaces. If we talk about the pressure distribution in the Y direction, Figures 20 to 22 show that for each dimple area density taken, bowtie-shaped dimple provides extremely steady pressure distribution than circular-shaped dimples and oriented bowtie-shaped dimples, which provides more stability in the Y direction as well.

5.4 Effect of Speed

The relationship between hydrodynamic pressure and sliding surface speed has frequently been proven. However, the hydrodynamic effects of speed in respect to dimples of various shapes may differ if one of the sliding surfaces is textured. Figure 23 shows the dimensionless pressure as a function of sliding speed for 3 different dimple shapes. Figure 23 makes it evident that, for all loading situations, the generated hydrodynamic pressure for all of the examined dimple shapes is nearly similar at a speed of 3 m/s but differs more as the speed increases.

Bowtie dimples and orientated bowtie dimples produce greater hydrodynamic pressure than circular dimples at 6 m/s, but the difference increases significantly at 9 m/s. At a sliding speed of 9 m/s, the pressure generated by a bowtie-shaped dimple is approximately 100% greater, while the pressure generated by an orientated bowtie-

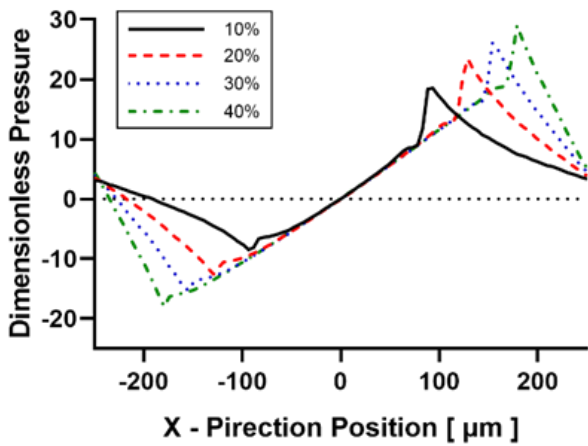


Figure 17: Effect of dimple area density on pressure distribution along x-direction (for circular dimple)

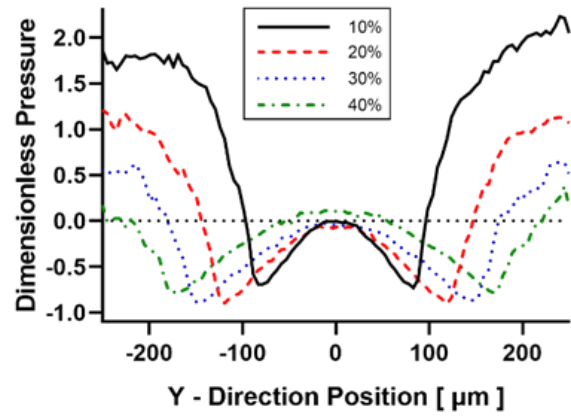


Figure 20: Effect of dimple area density on pressure distribution along y-direction (for circular dimple)

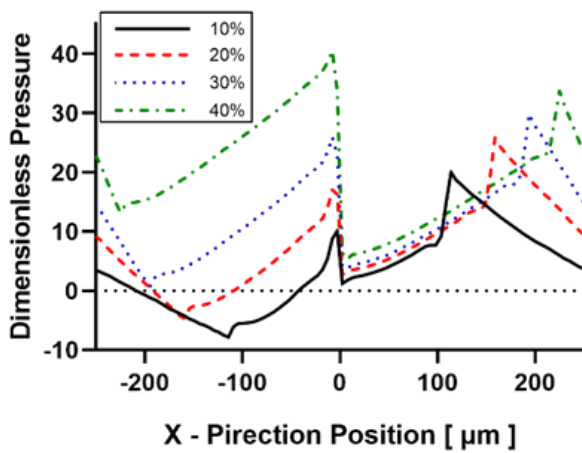


Figure 18: Effect of dimple area density on pressure distribution along x-direction (for bowtie dimple)

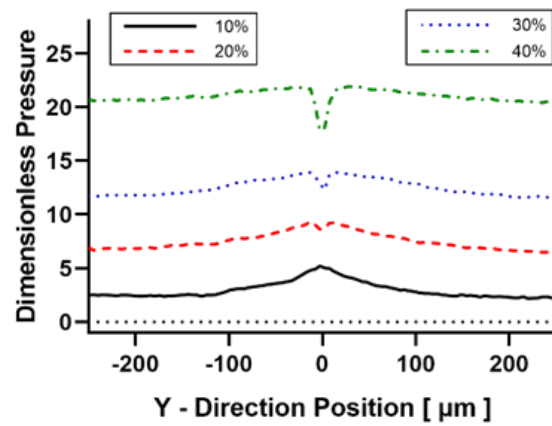


Figure 21: Effect of dimple area density on pressure distribution along y-direction (for bowtie dimple)

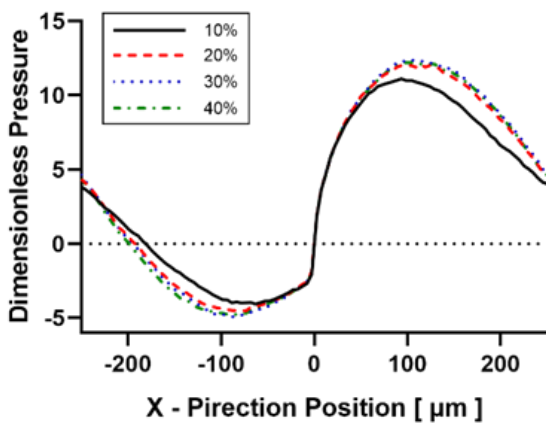


Figure 19: Effect of dimple area density on pressure distribution along x-direction (for oriented bowtie dimple)

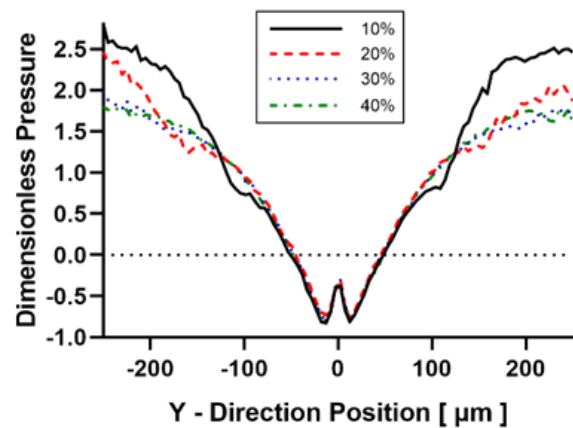


Figure 22: Effect of dimple area density on pressure distribution along y-direction (for oriented bowtie dimple)

shaped dimple is approximately 300% greater than the pressure generated by circular-shaped dimple. Thus, there is a large increase in the generation of hydrodynamic pressure and consequently tribological advantages if bowtie-shaped dimples or orientated bowtie-shaped dimples are employed as texturing rather than traditional circular-shaped dimples.

5.5 Experimental Results:

Figure 24 depicts the fluctuation in friction coefficient for circular, bowtie, and orientated bowtie-shaped dimples during various testing. For each dimple shape, the depth is assumed to be 30 μm, the area density is assumed to be 40%, and the RPM of the disc is assumed to be equivalent to a sliding speed of 6 m/s. The graph shows that the

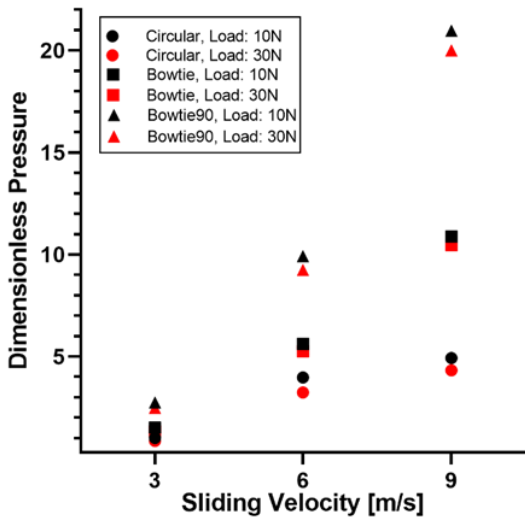


Figure 23: Dimensionless pressure as a function of sliding speeds

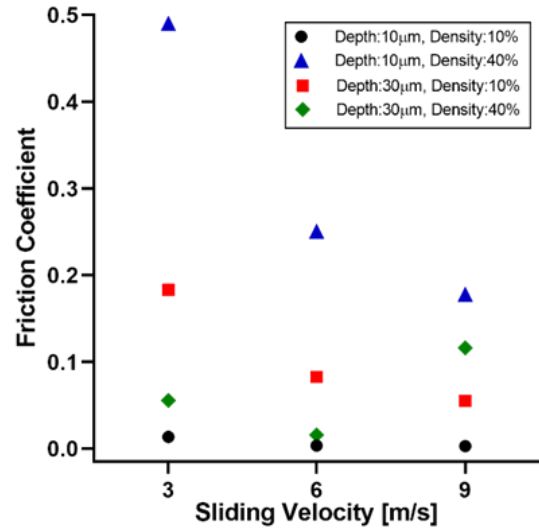


Figure 25: Friction coefficient as a function of sliding velocity for circular shaped dimple

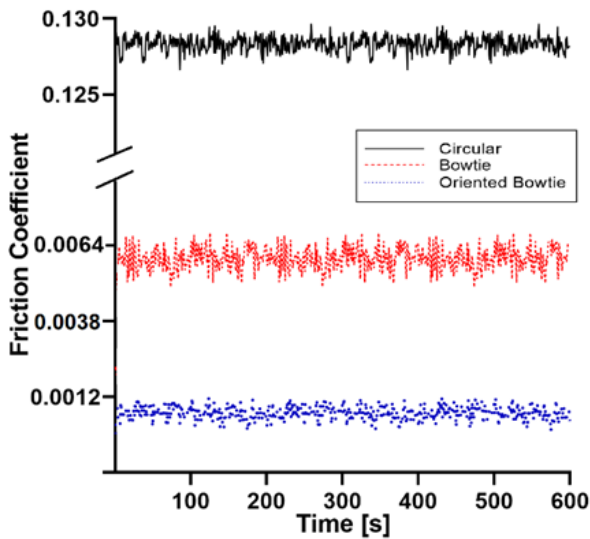


Figure 24: Variation of friction coefficient during different tests for different dimple shapes

friction coefficient for a dimple with a bowtie shape and oriented bowtie shape is significantly lower than the friction coefficient for a dimple with a circular shape. Therefore, it can be said that in sliding textured surfaces, bowtie-shaped and oriented bowtie-shaped dimples give higher tribological advantages than traditional circular-shaped dimples.

The influence of dimple depth and dimple area density on average friction coefficient for various dimple shapes under uniform loading conditions is shown in Figures 25 to 27. Dimple area density is assumed to be 10% and 40%, while dimple depth is assumed to be 10µm and 30µm. Thus, four outcomes are compared for each dimple shape at three distinct speeds. When can be seen, as the rotational speed rises, the average friction coefficient drops in the case of circular and oriented bowtie shaped dimples. The lubricant film is created by the textured surface, and film

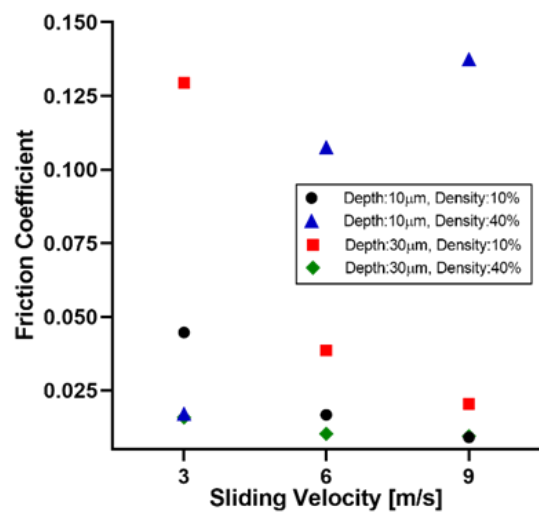


Figure 26: Friction coefficient as a function of sliding velocity for bowtie shaped dimple

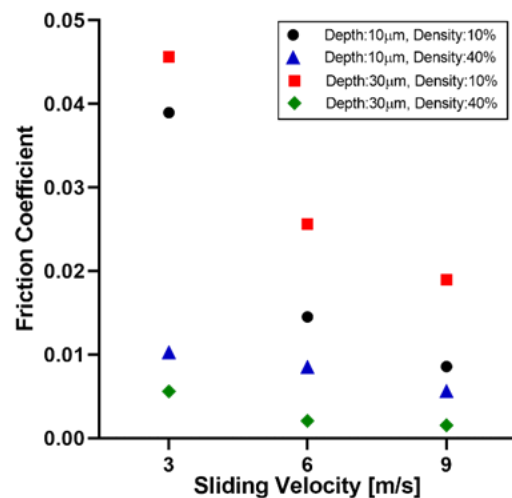


Figure 27: Friction coefficient as a function of sliding velocity for oriented bowtie shaped dimple

creation is significantly simpler at faster rotational speeds. But in the case of bowtie shaped dimple, for some reason, the opposite effect is being seen. On the other hand, it seems that dimple depth and dimple area density have a considerable impact on tribological performance.

For circular-shaped dimples at each speed, combinations of 10 μ m depth and 40% dimple area density result in the highest friction coefficient, while combinations of 10 μ m depth and 10% dimple area density result in the lowest friction coefficient. The friction coefficient for a dimple with a bowtie shape changes substantially with speed. When the speed is 3m/s, the maximum friction coefficient is found for a combination of a 30 μ m dimple depth and a 10% dimple area density, and the minimum friction coefficient is found for a combination of a 30 μ m dimple depth and a 40% dimple area density. However, when the speed is increased to 9m/s, the maximum friction coefficient is found for a combination of a 10 μ m dimple depth and a 40% dimple area density, and the minimum friction for oriented bowtie-shaped dimples, the combination of 30 μ m dimple depth and 40% dimple area density at 9m/s speed results in the lowest friction coefficient. For a combination of a 10 μ m dimple depth and a 10% dimple area density, bowtie-shaped dimples have the lowest friction coefficient of all the other forms that were taken into consideration at a velocity of 9m/s. These test findings exhibit good agreement with the CFD and numerical model results.

6. Conclusions

The effect of bowtie and orientated bowtie dimple shapes on circular dimple shapes to generate hydrodynamic pressure between two parallel sliding surfaces was investigated using CFD and numerical models. To assess the tribological performance of textured samples with all different types of dimples, pin on disc tests were next performed. Here is a summary of the results.

1. When the sliding speed, area density, and dimple depth are all the same, the oriented bowtie-shaped dimple produces the most hydrodynamic pressure of the three.

2. Dimple depth and dimple area density affect hydrodynamic pressure generation and tribological behavior. Bowtie-shaped dimples and oriented bowtie-shaped dimples generate hydrodynamic pressure better than circular-shaped dimples for each dimple depth and dimple area density taken for analysis.

3. For all loading situations, the generated hydrodynamic pressure for all of the examined dimple shapes is nearly similar at a speed of 3 m/s but differs more as the speed increases. Bowtie dimples and orientated bowtie dimples produce greater hydrodynamic pressure than circular dimples at 6 m/s, but the difference increases significantly at 9 m/s.

4. In the case of bowtie-shaped dimples and oriented bowtie-shaped dimples, the pressure is more uniformly distributed than in the case of circular-shaped dimples and hence bowtie and oriented bowtie dimples offer better

stability between the sliding surfaces. A bowtie-shaped dimple with 30 μ m dimple depth and 20% dimple area density gives maximum stability.

5. The friction coefficient also depends to a large extent on the shape of the dimple. Test findings exhibit good agreement with the CFD and numerical model results. It seems that dimple depth and dimple area density have a considerable impact on tribological performance.

6. When texturing is used to acquire a tribological advantage on sliding surfaces, unconventional (bowtie or oriented bowtie) shaped texturing is more effective under different test load, dimple depth, dimple area density and rotational speed conditions than typical circular texturing.

7. Acknowledgment

The authors are grateful to Government Engineering College, Gandhinagar, and Active Engineering Co., GIDC Vatva, Ahmedabad for providing resources and infrastructure support.

Nomenclature

x, y	Cartesian coordinates
X, Z	Non-dimensional Cartesian coordinates, $X = x/r_d$, $Z = z/r_d$
c	Clearance between parallel surfaces
r_i	Inner radius of the seal
r_o	Outer radius of the seal
p_{in}	Pressure at inner radius of the seal
p_{out}	Pressure at outer radius of the seal
$h(x,z)$	Local spacing
$H(X,Z)$	Non-dimensional local spacing, $H = h/c$
h_d	Dimple depth
p_a	Atmospheric pressure
p_{avg}	Average bearing pressure
$p(x,z)$	Bearing pressure
$P(X,Z)$	Non-dimensional pressure, $P = p/p_a$
$2r_l$	Length of the square unit cell
r_d	Dimple characteristic radius
S_d	Dimple area density
U	Sliding velocity
ϵ	Aspect ratio, $\epsilon = h_d/2r_d$
δ	Dimensionless minimum spacing, $\delta = c/2r_d$
μ	Dynamic viscosity
ξ	Film content parameter
K	Switch function
β	Bulk modulus of the lubricant
Λ	Dimensionless parameter, $\Lambda = 6\mu Ur_d/\beta c^2$

References

- [1] HAARDT, R. and GODET, M., "Axial vibration of a misaligned radial face seal under a constant closure force," ASLE Trans, 18, 1975, 55-61. <https://doi.org/10.1080/05698197508982747>
- [2] ETSION, I., "Squeeze effects in radial face seals," J. Lubric. Technol., 102, 1980, 145-152. <https://doi.org/10.1115/1.3251452>
- [3] SHARONI, A. and ETSION, I., "Performance of end-

- face seals with diametral tilt and coning-hydrodynamic effects," *ASLE Trans*, 24, 1978, 61-70. <https://doi.org/10.1080/05698198108982998>
- [4] LEBECK, A. O., TEALE, J. L., and PIERCE, R. E., "Hydrodynamic lubrication and wear in wavy contacting face seals," *J.Lubric. Technol.*, 100, 1978, 81-91. <https://doi.org/10.1115/1.3453120>
- [5] Ruddy, A. V., Dowson, D., and Taylor, C. M., "The prediction of film thickness in a mechanical face seal with circumferential waviness on both the face and the seat," *Journal of Mechanical Engineering Science*, 24, 1, 1982, 37-43. https://doi.org/10.1243/JMES_JOUR_1982_024_008_02
- [6] Key, W. E., Salant, R. F., Payvar, P., Gopalakrishnan, S., and Vaghasia, G., "Analysis of a Mechanical Seal with Deep Hydropads," *Tribology Transactions*, 32, 4, 1989, 481-489. <https://doi.org/10.1080/10402008908981916>
- [7] Nakano, M., Korenaga, A., and Korenaga, A., "Applying micro-texture to cast iron surfaces to reduce the friction coefficient under lubricated conditions," *Tribol. Lett.*, 28, 2007, 131-137. <https://doi.org/10.1007/s11249-007-9257-2>
- [8] Etsion, I., "State of the art in laser surface texturing," *J. Tribol.*, 127, 2005, 248-253. <https://doi.org/10.1115/1.1828070>
- [9] Voevodin, A. A., and Zabinski, J. S., "Laser surface texturing for adaptive solid lubrication," *Wear*, 261, 11-12, 2006, 1285-1292. <https://doi.org/10.1016/j.wear.2006.03.013>
- [10] Wang, X., Adachi, K., Otsuka, K., and Kato, K., "Optimization of the surface texture for silicon carbide sliding in water," *Appl. Surf. Sci.*, 253, 3, 2006, 1282-1286. <https://doi.org/10.1016/j.apsusc.2006.01.076>
- [11] Yan, D., Qu, N., Li, H., and Wang, X., "Significance of dimple parameters on the friction of sliding surfaces investigated by orthogonal experiments," *Tribol. Trans.*, 53, 2010, 703-712. <https://doi.org/10.1080/10402001003728889>
- [12] Etsion, I., and Burstein, L., "A model for mechanical seals with regular microsurface structure," *Tribol. Trans.*, 39, 1996, 677-683. <https://doi.org/10.1080/10402009608983582>
- [13] Etsion, I., Halperin, G., and Greenberg, Y., "Increasing mechanical seal life with laser-textured seal faces," In *Proc. of 15th international conference on fluid sealing BHR group*, Maastricht, 1997, 3-11.
- [14] Etsion, I., Kligerman, Y., and Halperin, G., "Analytical and experimental investigation of laser-textured mechanical seal faces," *Tribol. Trans.*, 42, 1999, 511-516. <https://doi.org/10.1080/10402009908982248>
- [15] Kligerman, Y., and Etsion, I., "Analysis of the hydrodynamic effects in a surface textured circumferential gas seal," *Tribol. Trans.*, 44, 3, 2001, 472-478. <https://doi.org/10.1080/10402000108982483>
- [16] Etsion, I., and Halperin, G., "A laser surface textured hydrostatic mechanical seal," *Tribol. Trans.*, 45, 3, 2002, 430-434. <https://doi.org/10.1080/10402000208982570>
- [17] Wang, X. L., and Hsu, S. M., 2004, "Integrated surface technology for friction control: A new paradigm effects of geometric shapes on friction," *The 4th china international symposium on tribology*, 2004, 12-20.
- [18] Yu, H., Wang, X., and Zhou, F., "Geometric shape effects of surface texture on the generation of hydrodynamic pressure between conformal contacting surfaces," *Tribol. Lett.*, 37, 2010, 123-130. <https://doi.org/10.1007/s11249-009-9497-4>
- [19] Bai, S., Peng, X., Li, Y., and Sheng, S., "A hydrodynamic laser surface-textured gas mechanical face seal," *Tribol. Lett.*, 38, 2, 2010, 187-194. <https://doi.org/10.1007/s11249-010-9589-1>
- [20] Yu, H., Deng, H., Haung, W., and Wang, X., "The effect of dimple shapes on friction of parallel surfaces," *Proceedings of the institution of mechanical engineers, Part J: Journal of engineering tribology*, 225, 8, 2011, 693-703. <https://doi.org/10.1177/1350650111406045>
- [21] Qiu, M., Delic, A., and Raeymaekers, B., "The effect of texture Shape on the load-carrying capacity of gas-lubricated parallel slider bearings," *Tribol. Lett.*, 48, 2012, 315-327. <https://doi.org/10.1007/s11249-012-0027-4>
- [22] Qiu, M., Minson, B., and Raeymaekers, B., "The effect of texture shape on the friction coefficient and stiffness of gas-lubricated parallel slider bearings," *Tribology International*, 67, 2013, 278-288. <https://doi.org/10.1016/j.triboint.2013.08.004>
- [23] Raeymaekers, B., Etsion, I., and Talke, F. E., "A model for the magnetic tape/guide interface with laser surface texturing," In *proceedings of the ASME/STLE international joint tribology conference*, 2008, 669-671. <https://doi.org/10.1115/IITC2007-44173>
- [24] Han, J., Fang, L., Sun, J., and Ge, S., "Hydrodynamic lubrication of microdimple textured surface using three-dimensional CFD," *Tribology Transactions*, 53, 6, 2010, 860-870. <https://doi.org/10.1080/10402004.2010.496070>
- [25] Han, J., Fang, L., Sun, J., Wang, Y., Ge, S., and Zhu, H., "Hydrodynamic lubrication of surfaces with asymmetric Microdimple," *Tribology Transactions*, 54, 4, 2011, 607-615. <https://doi.org/10.1080/1040200110402004.2010.496070>

doi.org/10.1080/10402004.2011.584364

- [26] Liu, W., Ni, H., Chen, H., and Wang, P., "Numerical simulation and experimental investigation on tribological performance of micro-dimples textured surface under hydrodynamic lubrication," *International Journal of Mechanical Sciences*, 163, 2019, 105095. <https://doi.org/10.1016/j.ijmecsci.2019.105095>
- [27] Wei, Y., Tomkowski, R., and Archenti, A., "Numerical study of the influence of geometric features of dimple texture on hydrodynamic pressure generation," *Metals*, 10, 361. <https://doi.org/10.3390/met10030361>
- [28] ANSYS Fluent Theory Guide, 2013.
- [29] Bakir, F., Rey, R., Gerber, A. G., Belamri, T., and Hutchinson, B., "Numerical and experimental investigations of the cavitating behaviour of an inducer," *Int. J. Totat. Mech.*, 10, 1, 2004, 15-25. <https://doi.org/10.1080/10236210490258034>
- [30] Cupillard, S., Glavatskih, S., and Cervantes, M. J., "Computational fluid dynamics analysis of a journal bearing with surface texturing. Proceedings of the Institution of Mechanical Engineers," *Part J: Journal of Engineering Tribology*, 222, 2, 2008, 97-107. <https://doi.org/10.1243/13506501JET319>